



Size-dependent selectivity and activity of CO₂ photoreduction over black nano-titanias grown on dendritic porous silica particles

Xiaoni Xuan^{a,1}, Shuchen Tu^{b,1}, Hongjian Yu^b, Xin Du^{a,*}, Yajing Zhao^c, Junhui He^c, Haifeng Dong^{a,*}, Xueji Zhang^{a,*}, Hongwei Huang^{b,*}

^a Research Center for Bioengineering and Sensing Technology, Beijing Key Laboratory for Bioengineering and Sensing Technology, Department of Chemistry & Biological Engineering, University of Science & Technology Beijing, Beijing 100083, China

^b School of Materials Science and Technology, China University of Geosciences, Beijing 100083, China

^c Functional Nanomaterials Laboratory, Technical Institute of Physics and Chemistry, Chinese Academy of Science, Beijing 100190, China



ARTICLE INFO

Keywords:

Dendritic porous silica
Black nano-titania
Photocatalysis
Carbon dioxide reduction
Size-dependent activity and selectivity

ABSTRACT

Titania (TiO₂) materials show great promising for photocatalytic CO₂ reduction into solar fuels. However, the CO₂ conversion efficiency of most TiO₂-based photocatalysts is still low up to now, which mainly results from their low accessible active surface areas and weak light-absorption ability. Herein, we employed dendritic porous silica nanospheres (DPSNs) with high accessible internal surface as carriers to successfully fabricate a series of efficient and robust DPSNs@X% TiO_{2-x} (X%: weight ratio of TiO₂/DPSNs) composite photocatalysts with tunable sizes of black TiO_{2-x} NPs. For CO₂ photocatalytic selectivity and activity, only CO was generated for 1–3 nm of small TiO_{2-x} NPs on DPSNs@X% TiO_{2-x} (X% ≤ 20%), while both CO and CH₄ were produced for 3–12 nm of larger TiO_{2-x} NPs on DPSNs@X% TiO_{2-x} (X% ≥ 40%). Noteworthily, DPSNs@80% TiO_{2-x} showed ultrahigh CH₄ production rate of 124.3 μmol g-TiO_{2-x}⁻¹ h⁻¹, moderate CO production rate of 14.7 μmol g-TiO_{2-x}⁻¹ h⁻¹ and high photocatalytic stability. The excellent photocatalytic performance should be attributed to be well-dispersed distribution, appropriate particle sizes, and suitable reduction degree of TiO_{2-x} NPs on the pore surface of DPSNs@80% TiO_{2-x} with high accessible specific surface area (208 m² g⁻¹). Furthermore, these characteristics lead to higher CO₂ adsorption capacity, much lower recombination rate of photogenerated electrons and holes, and enhanced carrier transfer and separation in black TiO_{2-x}, thus demonstrating dramatically high CO₂ photoreduction activity. This study may open new perspectives for the design of the supported photocatalysts, in which the morphologies and structures of the carriers are the key parameters.

1. Introduction

Owing to the ever-increasing consumption of fossil fuels in human activity, the emission of excessive carbon dioxide (CO₂) as a major cause of the greenhouse effect has attracted considerable concerns [1–12]. The effective conversion of CO₂ into value-added chemicals and clean fuels (CO, CH₄, methanol, etc.) should be an ideal method to simultaneously address the problems of both environmental and energy issues [1–12]. The solar light-driven CO₂ photocatalytic reduction may be an attractive, green and sustainable strategy to achieve it [1–12]. Among various materials, titania (TiO₂) undergoes the rapid growth as semiconductor photocatalysts for dye degradation, water splitting, CO₂ reduction, etc., due to its outstanding intrinsic features including facile

fabrication, environmental friendliness, abundant polymorphs, controllable nano/meso-structures, excellent chemical and thermal stability, and good electronic and optical properties [13–20]. However, due to the stability of CO₂ molecule, its photoreduction to yield CH₄ requires the participation of multiple protons and electrons. Hence, the CO₂ conversion efficiency of most TiO₂-based photocatalysts is still not very high up to now, which mainly results from their low accessible active surface areas and weak light-absorption ability [13–20].

Great effort has been devoted to overcome these two shortcomings via smart material design and surface engineering/modification [21–36]. On the one hand, in order to increase active surface areas with high accessibility, the introduction of mesopore or/and macropores with high permeability into bulk TiO₂ materials has become a common

* Corresponding authors.

E-mail addresses: duxin@mail.ipc.ac.cn, duxin@ustb.edu.cn (X. Du), hfdong@ustb.edu.cn (H. Dong), zhangxueji@ustb.edu.cn (X. Zhang), hhw@cugb.edu.cn (H. Huang).

¹ These authors contributed equally to this work.

Table 1
Experimental and structural parameters of products.

Sample	TTIP (mL)	Weight of uncalcined products (g)	Weight of calcined products (g)	TiO _{2-x} sizes (nm)	S _{BET} (m ² /g)	Pore Volume (cm ³ /g)	bandgap (eV) ^a
DPSNs@10% TiO _{2-x}	0.0373	ca. 0.1066	ca. 0.0962	1-2	314	1.15	2.75
DPSNs@20% TiO _{2-x}	0.0746	ca. 0.1131	ca. 0.1002	1-3	307	1.13	2.84
DPSNs@40% TiO _{2-x}	0.1492	ca. 0.1340	ca. 0.1249	3-6	285	1.1	2.86
DPSNs@60% TiO _{2-x}	0.2238	ca. 0.1599	ca. 0.1455	6-9	271	0.73	2.86
DPSNs@80% TiO _{2-x}	0.2984	ca. 0.1759	ca. 0.1627	8-12	208	0.57	2.98
DPSNs@100% TiO _{2-x}	0.3730	ca. 0.1920	ca. 0.1795	9-12	161	0.34	2.98
DPSNs@120% TiO _{2-x}	0.4476	ca. 0.2264	ca. 0.2104	9-12	148	0.31	2.98

^a Values obtained from UV-vis DR spectra.

strategy [21–25]. However, only pore surface elements are active, while the most untouched ones inside pore walls are inert. In addition, the introduction of too much porosity or too thin pore walls usually causes the instability of framework during multiple photocatalytic reactions. Moreover, it is difficult to control the sizes of small TiO₂ nanocrystals/nanoparticles (NPs), which the pore walls are composed of. On the other hand, traditional TiO₂ semiconductors have the limited optical absorption in the solar ultraviolet region due to their large electronic bandgaps of 3.2 eV for anatase TiO₂ [13–32]. Various surface modification strategies have been developed to narrow the bandgap, achieving the conversion of white TiO₂ into colorful ones for better optical absorption [26,22–36]. Noteworthily, the black TiO₂ with excellent light absorption ability in almost full optical spectrum has triggered world-wide research interest [26–31]. The black color is attributed to the introduction of Ti³⁺ or/and oxygen vacancies (Vo) in the disordered surface layer of TiO₂ (named as TiO_{2-x}), resulting in the remarkable decrease of bandgaps [26–31]. Improvement of the optical absorption properties demonstrated the enhanced photocatalytic activities. Therefore, in order to improve both the utilization efficiency of TiO₂ materials and their UV-vis light absorption ability for the enhanced CO₂ conversion efficiency, the smart combination of robust porous carriers with high accessible surface areas and ultrasmall black TiO_{2-x} NPs may be a feasible approach [21–36].

In this work, we employed dendritic porous silica nanospheres (DPSNs) as carriers to realize the controllable growth of amorphous TiO₂ for the construction of a series of efficient and robust DPSNs@X% TiO_{2-x} (X%: weight ratio of TiO₂/DPSNs) composite photocatalysts with tunable sizes of black TiO_{2-x} NPs, in order to simultaneously achieve high accessible active surface areas and strong light-absorption ability. DPSNs are employed as a catalyst carrier to load many small TiO_{2-x} NPs on the surface of center-radial pores with gradually increased pore sizes from particle center to surface. This aims to utilize their structural advantages of unique open three-dimensional (3D) dendrimer-like superstructures with center-radial large pore channels and a highly accessible internal surface area, as compared to conventional ordered mesoporous silica spheres with uniform pore sizes [37–43]. This type of pores with all/full/omni directions can allow for better diffusion of molecules than MCM-41 and SBA-15 type materials with only one direction, thus facilitating the functionalization of pore surface and the efficient loading of NPs on pore surface [37–43]. The sizes of black TiO_{2-x} NPs loaded on DPSNs can be easily tuned from 1–2 nm to 9–12 nm. And such a high X% of 80% just causes a slight loss of specific surface area, thus maintaining the high accessibility of TiO_{2-x} active sites. It is expected that these proposed DPSNs@X% TiO_{2-x} composites have an impressive CO₂ photoreduction conversion efficiency. In addition, we hypothesized that surface topology morphologies of DPSNs@X% TiO_{2-x} composites and the sizes of black TiO_{2-x} NPs would have important effect on photocatalytic activity and selectivity.

2. Experimental

2.1. Synthesis of DPSNs

Monodispersed DPSNs were facilely synthesized by using cetyltrimethylammonium tosylate (CTA-Tos) as a pore forming agent, 1-butyl-3-methylimidazolium trifluoro-methanesulfonate ([BMIM] OTF) as a co-structure directing agent, triethanolamine (TEA) as a mineralizing agent, water as a solvent and tetraethyl orthosilicate (TEOS) as a silica precursor [44,45]. A typical synthesis was conducted as follows: 0.96 g of CTA-Tos, 0.105 g of TEA, 0.3 g of [BMIM] OTF and 50 mL of water were mixed and stirred at 80 °C for 1 h. 7.8 mL of TEOS was rapidly injected into the surfactant solution. The mixture was stirred with a speed of 1000 rpm at 80 °C for another 2 h. The CTA-Tos and [BMIM] OTF were removed from particles by calcination. The as-prepared DPSNs were calcined at 550 °C for 5 h with a heating-up rate of 3 °C min⁻¹. The calcined DPSNs power has white color and is easily dispersed into alcohol.

2.2. Growth of TiO₂ on DPSNs to form DPSNs@X% TiO₂

TiO₂ was formed on the surface of center-radial pores of DPSNs by direct growth at solid-liquid hetero-interface. Typically, after 0.1 g of DPSNs was dispersed in 25 mL of ethanol under ultrasonic for 1 h, 12.5 mL of ethanol was added into the DPSNs suspension and allowed to stand under magnetic stirring for 10 min. Then, a given amount of titanium (IV) tetraisopropoxide (TTIP) was slowly added. After the mixture was kept for 12 h under intense stirring, 2.5 mL of ultra-pure water (0.5 mL min⁻¹) was slowly added into, and the final mixture kept on intense stirring for 2 h. The prepared product was gathered by centrifuging at 8000 rpm for 5 min, which was washed three times with the mixture of ethanol and ultra-pure water. Finally, the precipitate was dried at 60 °C and calcined at 550 °C for 5 h in Muffle furnace. The added amount of TTIP is regulated to achieve tunable weight ratios of TiO₂/DPSNs from 10% to 120% (Table 1). The obtained products were named as DPSNs@X% TiO₂, here X% means the weight ratios of TiO₂/DPSNs.

2.3. Reduction from DPSNs@X% TiO₂ to DPSNs@X% TiO_{2-x}

Hydrogen thermal reduction treatment in ambient pressure was carried out because it is a simple and straightforward way to use H₂ to reduce partial Ti⁴⁺ into Ti³⁺ on the surface of TiO₂ nanocrystals [46,47]. Typically, the prepared DPSNs@X% TiO₂ powder with white color was ground and placed in the ceramic crucible, on which a glass slide was covered with a vent of 2 mm on both sides. Then the powder was reduced in a tube furnace system with the gas flow (50 mL min⁻¹) of 5% H₂ and 95% Ar at 600 °C for 3 h at a heating rate of 5 °C min⁻¹. The obtained gray samples were named as DPSNs@X% TiO_{2-x}. It is worth to note that high temperature (400–700 °C) was commonly needed for ambient pressure H₂/Ar reduction, compared to that of high pressure H₂, due to its weaker reduction capability [29]. Thus, in order

to effectively reduce the DPSNs@X% TiO_{2-x}, 600 °C of high temperature was employed.

2.4. Photocatalytic test for CO₂ reduction

The photoreduction of CO₂ conversion was carried out by a Labsolar-III AG closed circulation system (Beijing Perfect light Technology Co., Ltd., China) [48,49]. 25 mg of DPSNs@X% TiO_{2-x} was ultrasonically dispersed in ultrapure water. Then, the suspension was spread evenly on the sample stage, which is located in the middle of the vacuum reactor. And a thin particle film with an area of ca. 1 cm² was formed after static drying. Subsequently, 5 mL of H₂SO₄ (4 mol L⁻¹) was transfused into the vacuum reactor to react with NaHCO₃ to obtain 1 atm of CO₂ gas. The reactor was irradiated by a 300 W Xe lamp (PLS-SXE300), and the photoreaction temperature was kept at 20 °C. The parameter of distance between Xe lamp and samples is fixed at 10 cm. The light intensity on the sample is measured to be about 0.5 W cm⁻² by Optical power meter. After reacted for given time, 1 mL of gas was taken out for subsequent qualitative analysis by GC9790II gas chromatography (Zhejiang Fuli Analytical Instrument Co.) with a thermal conductivity detector.

2.5. Characterization

The characterization methods were listed in the Supporting Information, including transmission electron microscopy (TEM), scanning electron microscopy (SEM), X-Ray powder diffraction (XRD), Fourier transform infrared (FTIR) spectra, Electron spin resonance (ESR) spectra, X-ray photoelectron spectroscopy (XPS), Raman spectra, photoluminescence (PL) emission spectra, time-resolved fluorescence decay spectra, UV-vis diffuse reflectance (UV-vis DR) spectra, nitrogen adsorption-desorption, and CO₂ adsorption. In situ diffuse reflectance infrared fourier transform spectroscopy (DRIFTS) was performed on the NICOLET iS50 FT-IR for measuring CO₂ adsorption/activation/conversion.

3. Results and discussion

3.1. Materials characterization: morphologies and structures

The schematic illustration of the fabrication strategy of a series of DPSNs@X% TiO_{2-x} composite photocatalysts with tunable sizes of TiO_{2-x} NPs is exhibited in Fig. 1. DPSNs are employed as a catalyst carrier to load many small TiO_{2-x} NPs on the surface of center-radial pores. TiO₂ can grow on the surface of center-radial pores via solid-liquid heterogeneous interface growth, and its loading

amount increases with increase of the addition amount of TiO₂ precursor. After calcination followed by H₂ thermal reduction treatment, black TiO_{2-x} NPs with tunable sizes are uniformly formed on DPSNs. In order to clarify the structures and morphologies of DPSNs@X

% TiO_{2-x}, several characterization tools were used, such as SEM, TEM, N₂ sorption, XRD, Raman spectroscopy, etc.

As shown in SEM and TEM images of Fig. 2a1–a3, the prepared DPSNs, which are formed by many wrinkled nanosheets (thickness: ca. 5–10 nm), have uniform geometric structures. These nanosheets are arranged from particle center to particle surface to constitute the radial pore channels, thus forming uniform spheres with particle sizes of 241 ± 28 nm. The formed center-radial large mesopores and macropores have an irregular slit-like porous structure with a wide surface pore size distribution of ca. 52 ± 26 nm. Nitrogen adsorption-desorption measurements show that DPSNs have a high BET surface area of 326 m² g⁻¹ and a high total pore volume of 1.26 cm³ g⁻¹.

Amorphous TiO₂ were loaded on the surface of center-radial pores of DPSNs by direct nucleation and growth at solid-liquid hetero-interface. The abundant Si-OH groups on DPSNs are beneficial for this growth by forming Si-O-Ti bond. With increase of the added TTIP amount from 0.0373 (i.e., X% = 10%) to 0.4476 mL (i.e., X% = 120%), the weight of product largely increases in proportion to X% (Table 1), indicating the complete hydrolysis and condensation of TTIP. The amount of the formed amorphous TiO₂ on DPSNs also gradually increases and no other unloaded TiO₂ species are found in the products (TEM images in Fig. S1), suggesting the efficient growth and loading of the formed TiO₂. After calcination under high temperature, the amorphous TiO₂ layer on DPSNs was changed into TiO₂ NPs due to thermal-induced crystallization and aggregation growth process. In addition, after H₂ reduction, the color of all products changes from white to gray (the mixture of black TiO_{2-x} and white silica color) (Fig. S2), indicating efficient reduction from TiO₂ to TiO_{2-x}.

As shown in the SEM and TEM images of Fig. 2, a lot of small TiO_{2-x} NPs uniformly loaded on the surface of center-radial large pores of DPSNs with high distribution density. Moreover, the size of TiO_{2-x} NPs on the DPSNs continuously increases from 1–2 to 8–12 nm with the increase of the initially added TTIP amount from 0.0373 to 0.2984 mL, while their distribution density gradually decreases due to the formation of larger TiO_{2-x} NPs. It is worth to note that the TiO_{2-x} NPs still maintain similar sizes of 9–12 nm even with further increase of TTIP from 0.2984 to 0.4476 mL. Accordingly, the thickness of wrinkled nanosheets of DPSNs gradually increases due to the attachment of more TiO_{2-x}. During 0–60% of X%, the DPSNs@X% TiO_{2-x} composites can still maintain the center-radial large pores (Fig. 2a1–e3). However, at X% = 80%, some center-radial large pores of DPSNs@80% TiO_{2-x} composite are partially filled by TiO_{2-x} NPs (Fig. 2f1–f3). TiO_{2-x} NPs completely fill center-radial large pores, and some TiO_{2-x} NPs appear on the surface of DPSNs at X% = 100% (Fig. 2g1–g3). At X% ≥ 120%, some TiO_{2-x} NPs are separated from DPSNs@120% TiO_{2-x} (Fig. S3), due to the excessive TTIP addition. To the best of our knowledge, this is the first report about the well-dispersed loading of ultrafine TiO_{2-x} NPs (size: 1–2 nm) by controlling the hetero-interface growth.

The pore structures of all DPSNs@X% TiO_{2-x} were also

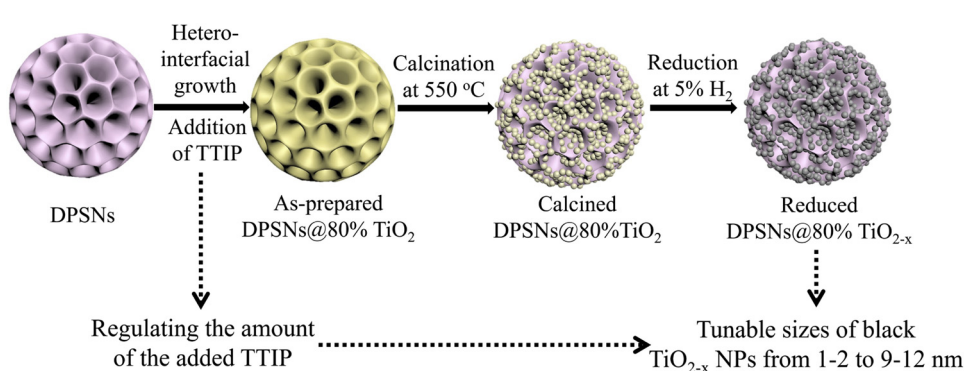


Fig. 1. Schematic illustration of the fabrication process of DPSNs@X% TiO_{2-x} with tunable TiO_{2-x} sizes by controlling the amount of the added TTIP.

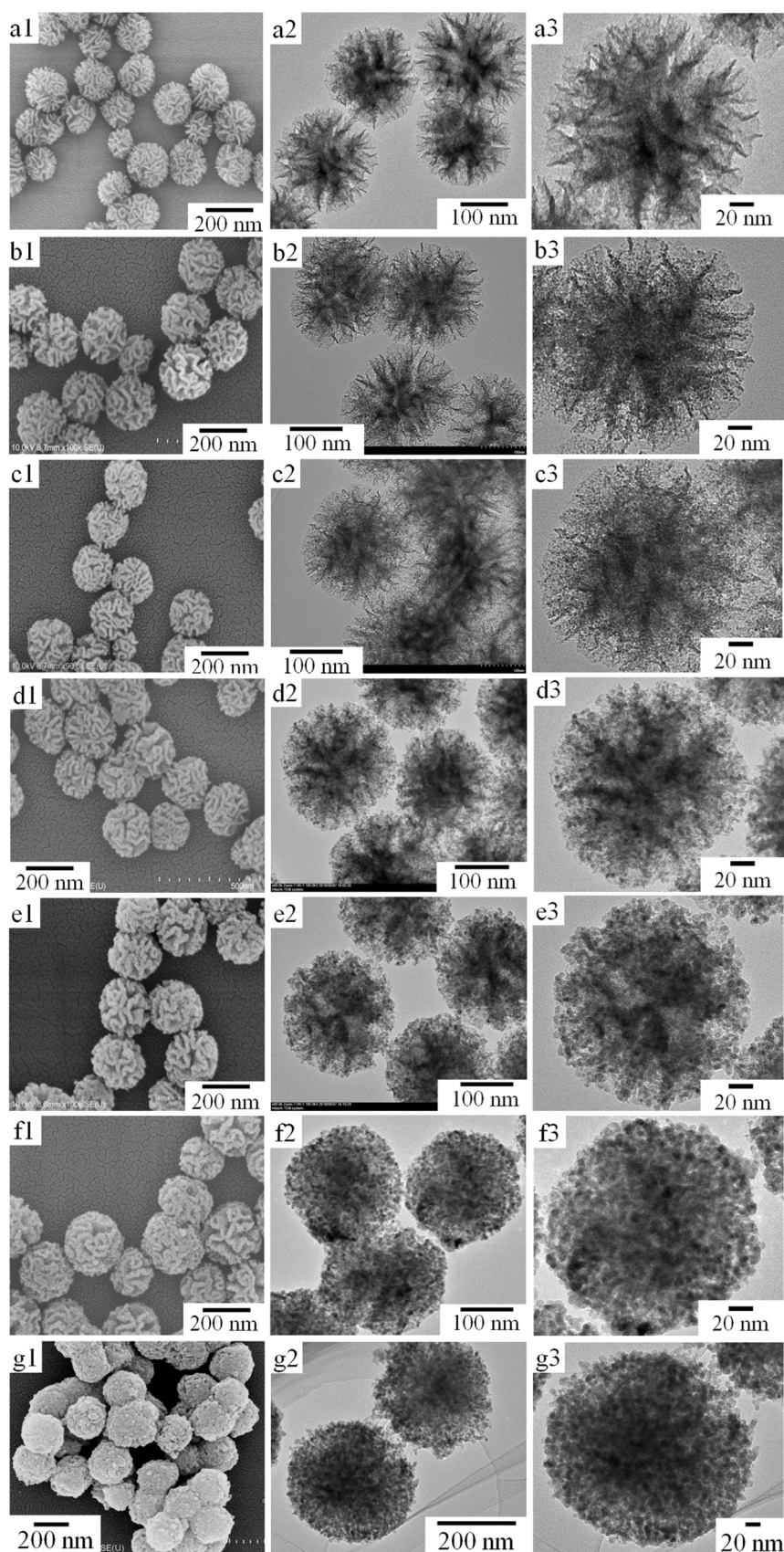


Fig. 2. SEM and TEM images of DPSNs (a1-a3), DPSNs@10% $\text{TiO}_{2-\text{x}}$ (b1-b3), DPSNs@20% $\text{TiO}_{2-\text{x}}$ (c1-c3), DPSNs@40% $\text{TiO}_{2-\text{x}}$ (d1-d3), DPSNs@60% $\text{TiO}_{2-\text{x}}$ (e1-e3), DPSNs@80% $\text{TiO}_{2-\text{x}}$ (f1-f3) and DPSNs@100% $\text{TiO}_{2-\text{x}}$ (g1-g3).

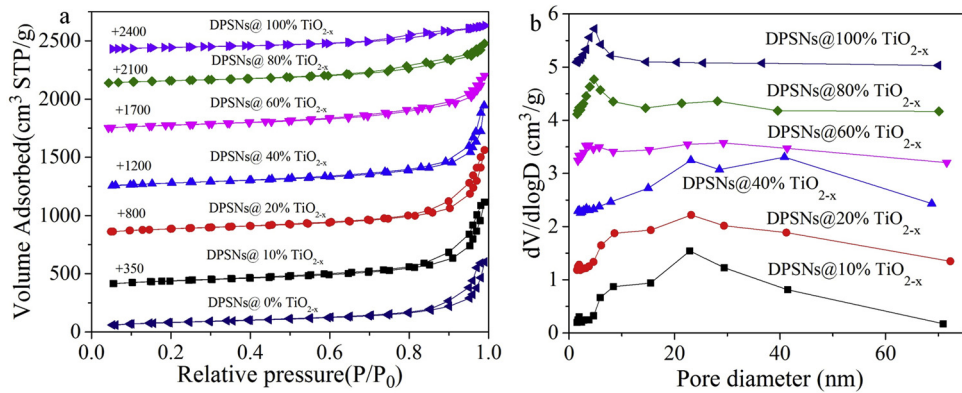


Fig. 3. (a) N₂ adsorption-desorption isotherms of all DPSNs@X% TiO_{2-x} and (b) the corresponding BJH pore size distribution curves.

characterized by N₂ adsorption-desorption measurement (Fig. 3a). As shown in BJH pore size distribution curves (Fig. 3b), with the increase of the initially added TTIP amount, ca. 5–50 nm of large mesopores (wide strong peak) of DPSNs@10% TiO_{2-x} gradually change to ca. 2–15 nm of small mesopores (narrow strong peak) and 15–40 nm of large mesopores (wide weak peak) of DPSNs@80% TiO_{2-x}, and finally to only ca. 2–15 nm of small mesopores of DPSNs@100% TiO_{2-x}. Simultaneously, both their BET specific surface areas and total pore volumes continuously decrease from 314 to 148 m² g⁻¹, and from 1.14 to 0.31 cm³ g⁻¹ (Table 1), respectively. These results are largely consistent with those from SEM and TEM images (Fig. 2), suggesting the existence of more TiO_{2-x} NPs on the surface of center-radial pores at higher X%. In addition, such a high X% just causes a modest loss of specific surface areas. And these values of specific surface areas are still higher than those of many ordered mesoporous TiO₂ materials [21–25,50–52].

Fig. 4a shows the XRD patterns of all DPSNs@X% TiO_{2-x}. During X% ≥ 40 wt.%, the XRD patterns of these products exhibit five diffraction peaks at 2θ = 25.4°, 38.1°, 48.2°, 54.8°, and 63.0° (Fig. 4a), which are ascribed to the (101), (004), (200), (211), and (204) crystalline planes

of the anatase phase of TiO₂ (JCPDS card no. 21-1272), respectively, and a very broad peak at 2θ = 23.0° is assigned to amorphous silica. The phase change from anatase to rutile did not occur at a high temperature (600 °C for 3 h) in the gas flow of 5% H₂ and 95% Ar, which may be attributed to be that anatase TiO_{2-x} NPs were stabilized by surface adsorbed hydrogen, while rutile NPs were stabilized by surface adsorbed oxygen [46,53]. Moreover, with the increase of X%, the intensity of diffraction peaks increases. The average crystal sizes of TiO_{2-x} NPs on DPSNs@40% TiO_{2-x}, DPSNs@60% TiO_{2-x}, DPSNs@80% TiO_{2-x} and DPSNs@100% TiO_{2-x} are calculated to be ca. 3.1, 5.3, 7.7 and 7.8 nm, respectively, by using Scherrer's formula based on the major (101) diffraction peak. Raman spectra in Fig. 4b reveal four peaks, which belong to the typical TiO₂ anatase Raman bands. For gray DPSNs@80% TiO_{2-x}, the strongest peak at ca. 144.2 cm⁻¹ shows a visible broadening as well as a blue shifting to 146.2 cm⁻¹ compared with white DPSNs@80% TiO₂. This phenomenon reported in the literatures was ascribed to Vo or Ti³⁺ centers on the TiO_{2-x} surface [54,55]. High Resolution TEM (HRTEM) images in Fig. 4c,d show the well-dispersed distribution of many small TiO_{2-x} NPs (sizes: 6–9 nm) with clear crystal lattices on DPSNs@60% TiO_{2-x}, and the sizes of most

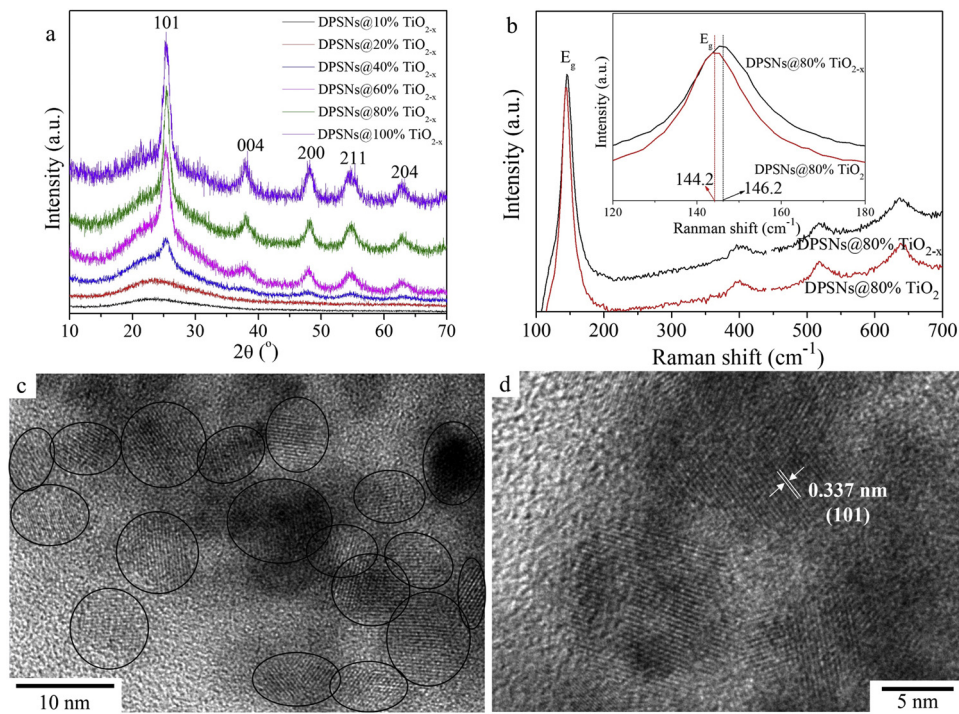


Fig. 4. (a) XRD patterns of all DPSNs@X% TiO_{2-x}. (b) Raman spectra of DPSNs@80% TiO₂ and DPSNs@80% TiO_{2-x}. (c,d) HRTEM images of DPSNs@60% TiO_{2-x}. Black circles in (c) point out the TiO_{2-x} NPs with clear crystal lattices.

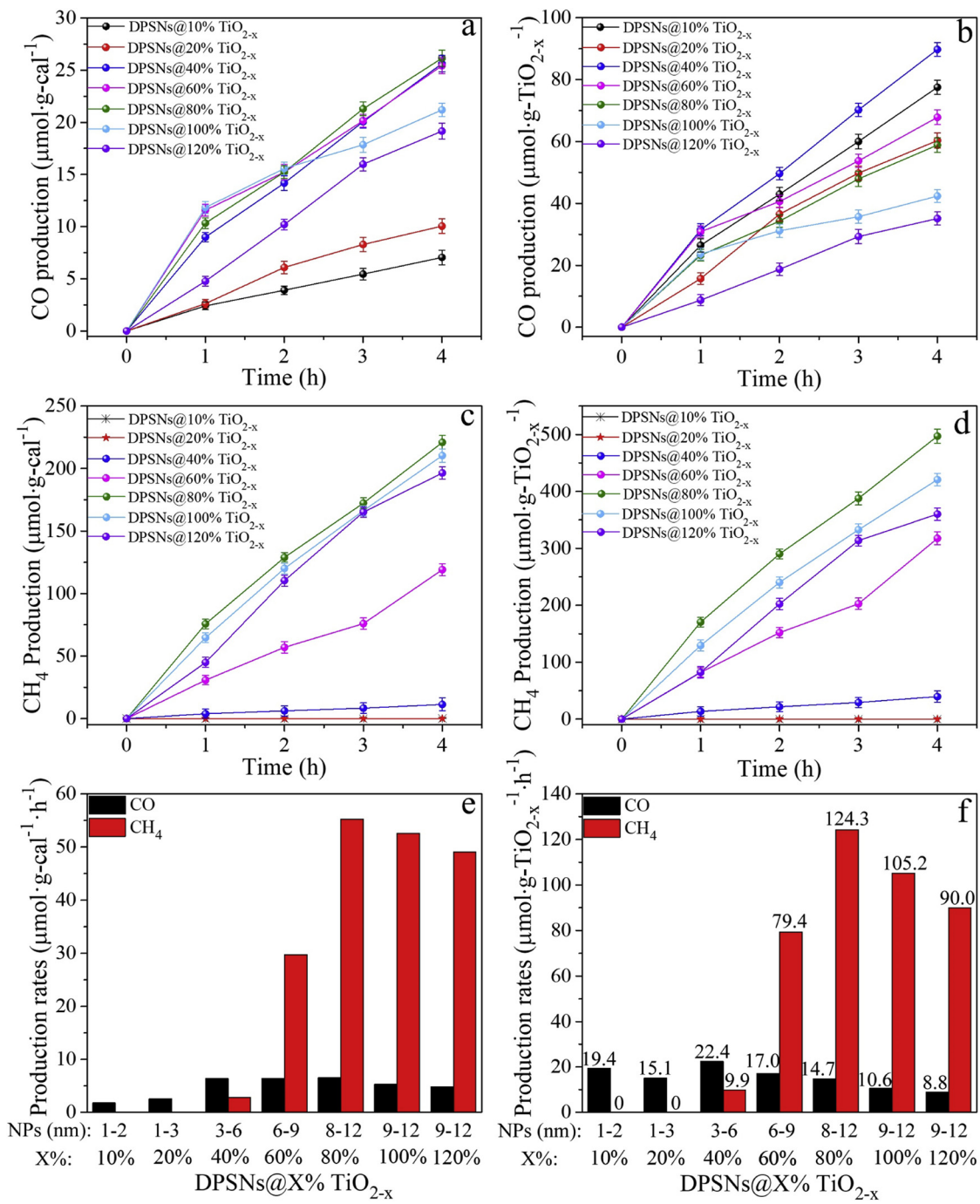


Fig. 5. (a-d) Time-dependent CO and CH₄ production and (e,f) their apparent rate constants for CO₂ photoreduction over (a,c,e) whole DPSNs@X% TiO_{2-x} and (b,d,f) TiO_{2-x} components on DPSNs@X% TiO_{2-x} under the irradiation of a 300 W Xe lamp.

exposed crystal lattices are measured to be ca. 0.337 nm, in accordance with (101) diffraction peak of TiO₂ anatase phase. Noteworthily, the thin disordered surface layer, which was often reported in the previous studies [26–31,56], cannot be clearly found on the surface of the crystalline TiO_{2-x} core, suggesting low reduction extent. During X% ≤ 20%, no TiO₂ diffraction peaks appear in XRD patterns (Fig. 4a), and no obvious TiO_{2-x} NPs with clear crystal lattices can be observed in HRTEM image (Fig. S4). The reason may be attributed to the extremely small sizes (1–2 nm) and lower contents of TiO_{2-x} NPs.

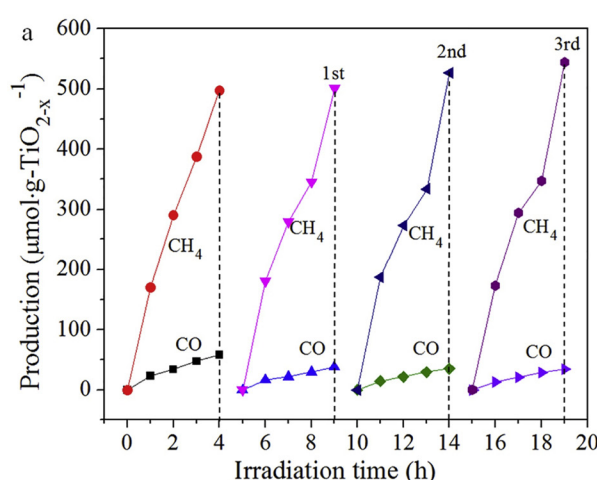
3.2. CO₂ photocatalytic reduction

The CO₂ photoreduction was carried out to study the photocatalytic

activity of a series of DPSNs@X% TiO_{2-x} with tunable sizes of TiO_{2-x} NPs under the irradiation of a 300 W Xe lamp. Background tests by purging argon and without adding NaHCO₃ in the reaction cell were first performed. No CO₂ conversion products (CO or CH₄) were detected for all DPSNs@X% TiO_{2-x} in the gas chromatograms (Fig. S5), and FTIR spectra in Fig. S6 only show typical Si-O-Si and Ti-O-Ti peaks. Thus, it indicates that the conversion products were not derived from residue organics in the catalysts. Fig. 5 shows the production amounts (in unit of μmol·g·cat⁻¹ (a,c) and μmol·g·TiO_{2-x}⁻¹ (b,d)) and production rates (in unit of μmol·g·cat⁻¹ h⁻¹ (e) and μmol·g·TiO_{2-x}⁻¹ h⁻¹ (f)) of CH₄ and CO as a function of irradiation time for all DPSNs@X% TiO_{2-x} products. Almost linearity formation amounts on CH₄ and CO evolution can be observed (Fig. 5a-d), which indicates the stability of our CO₂

photoreduction process and photocatalysts. For CO production rates, DPSNs@40% TiO_{2-x} perform the highest one among all these products (Fig. 5f), with 22.4 $\mu\text{mol g-TiO}_{2-x}^{-1} \text{ h}^{-1}$. For CH₄ production rates, no CH₄ is detected for both DPSNs@10% TiO_{2-x} and DPSNs@20% TiO_{2-x}. Furthermore, CH₄ production rate shows an increasing trend with increase of X% from 40 to 80%, while it decreases when X% further increases to $\geq 100\%$. Thus, DPSNs@80% TiO_{2-x} possess the highest CH₄ production rate of 124.3 $\mu\text{mol g-TiO}_{2-x}^{-1} \text{ h}^{-1}$ among all these products (Fig. 5f). In addition, it is meaningful to normalize the production rate constants of DPSNs@X% TiO_{2-x} products with their BET specific surface areas (Table 1). As shown in Fig. S7, DPSNs@40% TiO_{2-x} have the highest normalized CO production rate of 0.079 $\mu\text{mol g-TiO}_{2-x}^{-1} \text{ m}^2 \text{ h}^{-1}$, while DPSNs@100% TiO_{2-x} possess the highest normalized CH₄ one of 0.65 $\mu\text{mol g-TiO}_{2-x}^{-1} \text{ m}^2 \text{ h}^{-1}$. In order to further evaluate the photocatalytic activity of DPSNs@80% TiO_{2-x}, its solar-to-CO&CH₄ conversion efficiency and apparent photochemical Quantum Efficiency are calculated to be ca. 0.065% and 0.37%, respectively, based on the equations in supporting information. Noteworthily, during X% $\leq 20\%$, CO₂ is only photo-reduced into CO. In comparison, during X% $\geq 40\%$, the photocatalytic products of CO₂ are both CO and CH₄, indicating that large TiO_{2-x} NPs with high crystallization degree are beneficial to the generation of CH₄. These interesting results indicate that these DPSNs@X% TiO_{2-x} composites have the distinctly different photocatalytic activity and selectivity, which should be attributed to different surface topology morphologies, the sizes of black TiO_{2-x} NPs and photoreduction degree of TiO_{2-x} NPs' surface during H₂ thermal reduction treatment (discussed in detail later).

The photocatalytic stability is another significant factor for practical application besides photocatalytic performance. Three-run cycling experiments of CO₂ photoreduction were carried out to inspect it. As exhibited in Fig. 6a, there is not even a slight shrinkage of photocatalytic activity for DPSNs@80% TiO_{2-x} after three successive cycles. In addition, abnormally, the yield of CH₄ suddenly increases a little in fourth hour in each cycling experiments. TEM images of DPSNs@80% TiO_{2-x} before and after three cycle reactions do not show any difference (Fig. 6b–e). These results indicate the superior stability of these DPSNs@X% TiO_{2-x} photocatalysts. The reason is still unclear for this abnormal increase of CH₄ yield in fourth hour of each cycling experiments. It may be ascribed to long-time irradiation of UV light in Xe lamp, which may cause the formation of more Vo and/or Ti³⁺ on the surface of TiO_{2-x} NPs, thus promoting the photocatalytic reactions. When the irradiation is stopped, the oxygen in air may oxidize the newly formed Vo and/or Ti³⁺. Due to the lack of equipment for in situ Vo and Ti³⁺ characterization, we hope to carry out the in-depth study in the near future.



H₂ thermal reduction treatment of TiO₂ NPs and their reduction degrees should have an important impact on photocatalytic performance. As shown in Fig. S8, DPSNs@20% TiO_{2-x} show higher CO production rate ($\mu\text{mol g-TiO}_{2-x}^{-1} \text{ h}^{-1}$: 16.6 vs. 11.4) than DPSNs@20% TiO₂, indicating that TiO_{2-x} NPs can enhance the CO₂ photoreduction activity. In addition, DPSNs@X% TiO_{2-x} with higher reduction degrees can be obtained by controlling H₂ reduction treatment conditions [23–28]. It can be found from Fig. S9a-d that the strongest peak is located at ca. 146.2 cm⁻¹ for DPSNs@80% TiO_{2-x} with gray color, while it shows a bigger blue shifting to 154.3 cm⁻¹ for DPSNs@60% TiO_{2-x} with deeper color. It indicates that DPSNs@60% TiO_{2-x} with deeper color have higher reduction degree. The CO and CH₄ production rates of DPSNs@60% TiO_{2-x} with deeper color are 8.3 and 73.3 $\mu\text{mol g-TiO}_{2-x}^{-1} \text{ h}^{-1}$, respectively, which are lower than those (17.4 and 79.4 $\mu\text{mol g-TiO}_{2-x}^{-1} \text{ h}^{-1}$) of DPSNs@60% TiO_{2-x} with gray color (Fig. S9e–j). It indicates that the higher reduction degree on the surface of TiO_{2-x} NPs may be unfavorable for the transportation of photogenerated carriers, thus resulting in lower photocatalytic activity.

To investigate the visible-light induced photocatalytic activity, a filter (≥ 420 nm) is fixed on a 300 W Xe lamp. As shown in Fig. S10, there are not any CO and CH₄ products for DPSNs@100% TiO₂, while there is only a small amount of CO product (2.9 $\mu\text{mol g-TiO}_{2-x}^{-1}$ in 4 h) for DPSNs@100% TiO_{2-x}. It suggests that high CO₂ photoreduction activity of DPSNs@X% TiO_{2-x} should mainly result from UV (< 420 nm)-light activated photocatalysis.

There have been many reports about the impressive photocatalytic H₂ evolution performance of black titatias up to now [26–31]. Thus, it is also necessary to investigate photocatalytic H₂ evolution activity of DPSNs@X% TiO_{2-x} without Pt loading. By adding lactic acid as the sacrificial agent, under the irradiation of 300 W Xe lamp, there is almost no H₂ production for DPSNs@10% TiO_{2-x}. In contrast, the apparent rate constant of H₂ production of DPSNs@80% TiO_{2-x} is ca. 21.0 $\mu\text{mol g-TiO}_{2-x}^{-1} \text{ h}^{-1}$ (Fig. S11), which is lower than those in most literatures and its CH₄ production rate of 124.3 $\mu\text{mol g-TiO}_{2-x}^{-1} \text{ h}^{-1}$ [26–31]. It indicates that DPSNs@X% TiO_{2-x} have the relatively weak photocatalytic H₂ production ability compared with CO₂ photoreduction.

3.3. Investigation of photocatalytic activity enhancement mechanism

As shown in Table S1, without Pt deposition/loading, our developed DPSNs@X% TiO_{2-x} samples, especially DPSNs@80% TiO_{2-x}, show much more enhanced CO₂ photocatalytic activity than those in the literatures [13–36]. The intrinsic mechanism of CO₂ photocatalytic reduction is very complex. The photocatalytic performance of photocatalysts is always closely related to their final properties (band structures, UV-vis

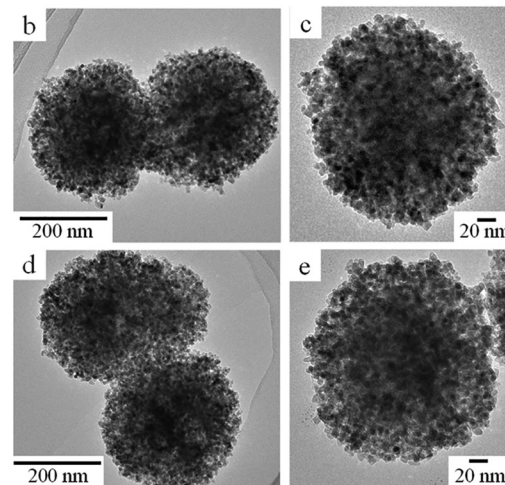


Fig. 6. (a) Cycling runs for CO₂ reduction over DPSNs@80% TiO_{2-x}. TEM images of DPSNs@80% TiO_{2-x} before (b,c) and after (d,e) three cycling runs.

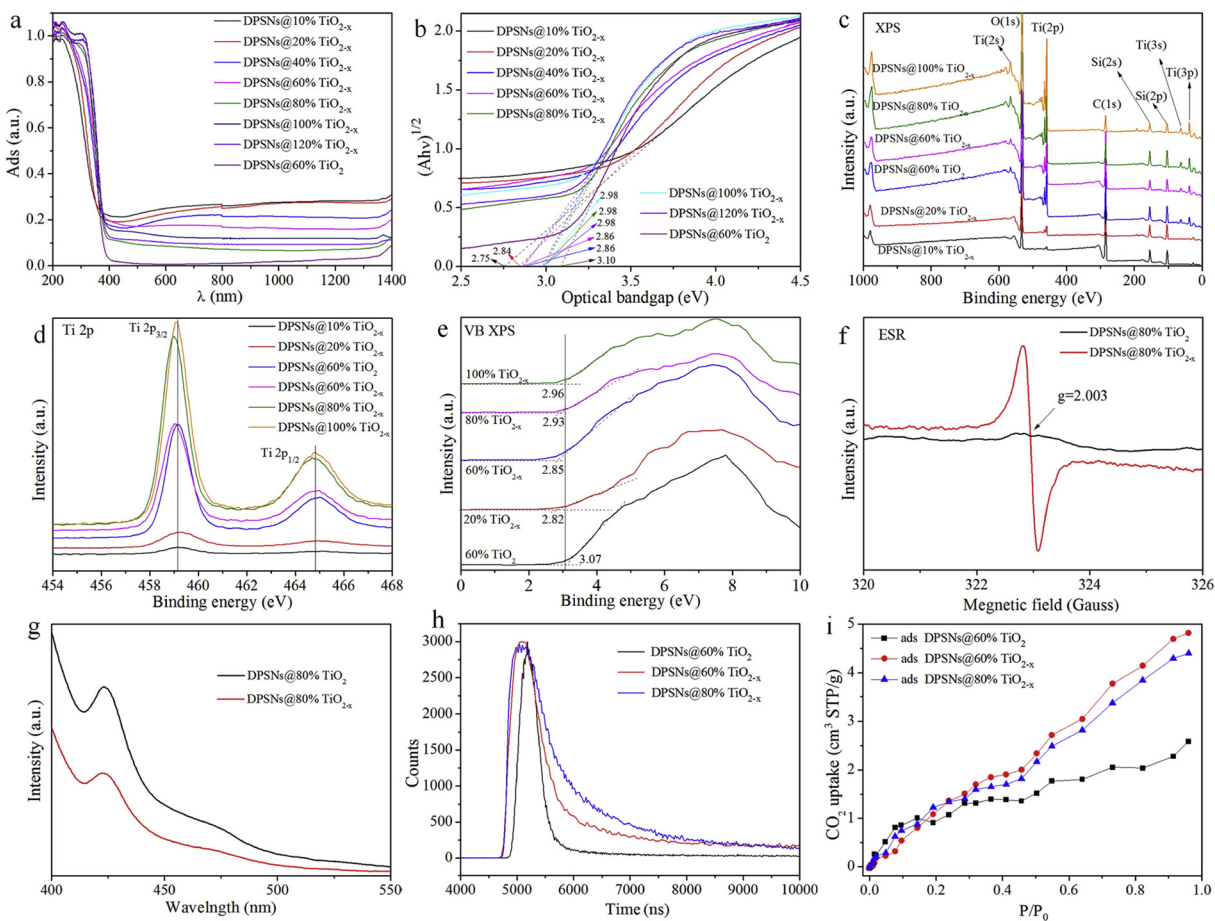


Fig. 7. (a) UV-vis DR spectra and (b) the corresponding optical bandgaps of DPSNs@X% $\text{TiO}_{2-\text{x}}$. (c) XPS full and (d) Ti 2p spectra of DPSNs@60% TiO_2 , DPSNs@60% $\text{TiO}_{2-\text{x}}$ and DPSNs@80% $\text{TiO}_{2-\text{x}}$. Note that C element in (a) is from atmosphere. (e) VB XPS spectra of DPSNs@60% TiO_2 and DPSNs@X% $\text{TiO}_{2-\text{x}}$. (f) ESR spectra, (g) PL spectra and (h) time-resolved fluorescence decay spectra of DPSNs@80% TiO_2 and DPSNs@80% $\text{TiO}_{2-\text{x}}$. (h) CO_2 adsorption isotherms on DPSNs@60% TiO_2 , DPSNs@60% $\text{TiO}_{2-\text{x}}$ and DPSNs@80% $\text{TiO}_{2-\text{x}}$ at 75 °C.

light absorption, charge separation, specific surface area), which are often affected by $\text{TiO}_{2-\text{x}}$ particle sizes, shape, morphology, doping, surface facet, defect content, etc [21,14–36].

UV-vis DR spectra in Figs. 7a,b and S12 reveal that all DPSNs@X% $\text{TiO}_{2-\text{x}}$ products have a stronger absorption in the vis-NIR region than DPSNs@X% TiO_2 , and their optical bandgap values are lower than that (3.10 eV) of DPSNs@60% TiO_2 . It should result from that the introduction of Ti^{3+} ions or/and Vo shortens the optical bandgap of TiO_2 , leading to the improvement of light absorption [26–31,51–57]. In addition, with the increase of X% from 10% to 80%, their vis-NIR absorption intensity decreases, and their optical bandgap slightly shifts to a higher energy from 2.75 to 2.98 eV. However, further increase of X% from 80% to 120% does not cause a further shift of bandgap to a higher energy. It may be attributed to be that the smaller sizes of $\text{TiO}_{2-\text{x}}$ NPs are more easily to be reduced (i.e., higher reduction degree) under identical H_2 thermal reduction condition, while 8–12 nm of $\text{TiO}_{2-\text{x}}$ NPs should have similar reduction degrees. The introduction of Ti^{3+} or/and Vo narrows the bandgap of $\text{TiO}_{2-\text{x}}$, thus enhancing the vis-NIR light absorption ability. However, it also weakens the reduction power of electrons [20,58,59].

XPS is a powerful tool to study the change of surface chemical bonding. As shown in Fig. 7c, Si, O and Ti elements exist in DPSNs@X% TiO_2 and DPSNs@X% $\text{TiO}_{2-\text{x}}$, and the peak intensity values of both Ti 2p and O 1s connected with Ti increase with increase of X% (Fig. S13). Noteworthily, DPSNs@60% TiO_2 and DPSNs@X% $\text{TiO}_{2-\text{x}}$ samples show only Ti 2p_{1/2} and Ti 2p_{3/2} peaks, but no Ti^{3+} peaks. Compared with DPSNs@60% TiO_2 , very slightly blue shift of binding energy positions

occurs for DPSNs@60% $\text{TiO}_{2-\text{x}}$, DPSNs@80% $\text{TiO}_{2-\text{x}}$, and DPSNs@100% $\text{TiO}_{2-\text{x}}$ (Fig. 7d), which may be ascribed to the existence of Vo or/and Ti^{3+} [51,60]. In comparison, no such shift appears for DPSNs@10% $\text{TiO}_{2-\text{x}}$ and DPSNs@20% $\text{TiO}_{2-\text{x}}$, which may result from very weak peak intensity caused by low TiO_2 content. The valence band (VB) XPS spectra were employed to study the effect of hydrogenation on the electronic band structure of TiO_2 NPs on DPSNs (Fig. 7e) [26–31]. The VB spectrum of DPSNs@60% TiO_2 shows the characteristic density of states of TiO_2 . However, after hydrogenation, a slight blue shifts of the absorption edges of $\text{TiO}_{2-\text{x}}$ appear on DPSNs@X% $\text{TiO}_{2-\text{x}}$, suggesting the defects-induced VB mid-gap positions with lower energy. And this value seems to gradually decrease with the decrease of X%, suggesting that smaller NPs may have more Vo .

As a very sensitive tool to probe paramagnetic species with unpaired electrons, ESR has been widely used to prove the existence of Vo and Ti^{3+} [26–31]. Before ESR measurement, the DPSNs were removed from DPSNs@X% TiO_2 by selective etching with NaOH solution in order to avoid the effect of silica species. The pristine TiO_2 in DPSNs@80% $\text{TiO}_{2-\text{x}}$ shows no recognizable resonance signal, suggesting the absence of Vo and Ti^{3+} , as shown in Fig. 7f. In comparison, a strong ESR peak at a g value of 2.003 is observed in the $\text{TiO}_{2-\text{x}}$ in DPSNs@80% $\text{TiO}_{2-\text{x}}$, indicating the existence of Vo trapped with an electron [29]. However, there was no obvious signal response at $g = 1.94\text{--}1.99$, which is usually a typical signal of the Ti^{3+} species. This result indicates that Vo should be generated after hydrogenation, while no Ti^{3+} species exist [29]. This is reasonable because ambient pressure $\text{H}_2\text{-Ar}$ treatment has a low reduction ability to generate the Ti^{3+} species, which is much more

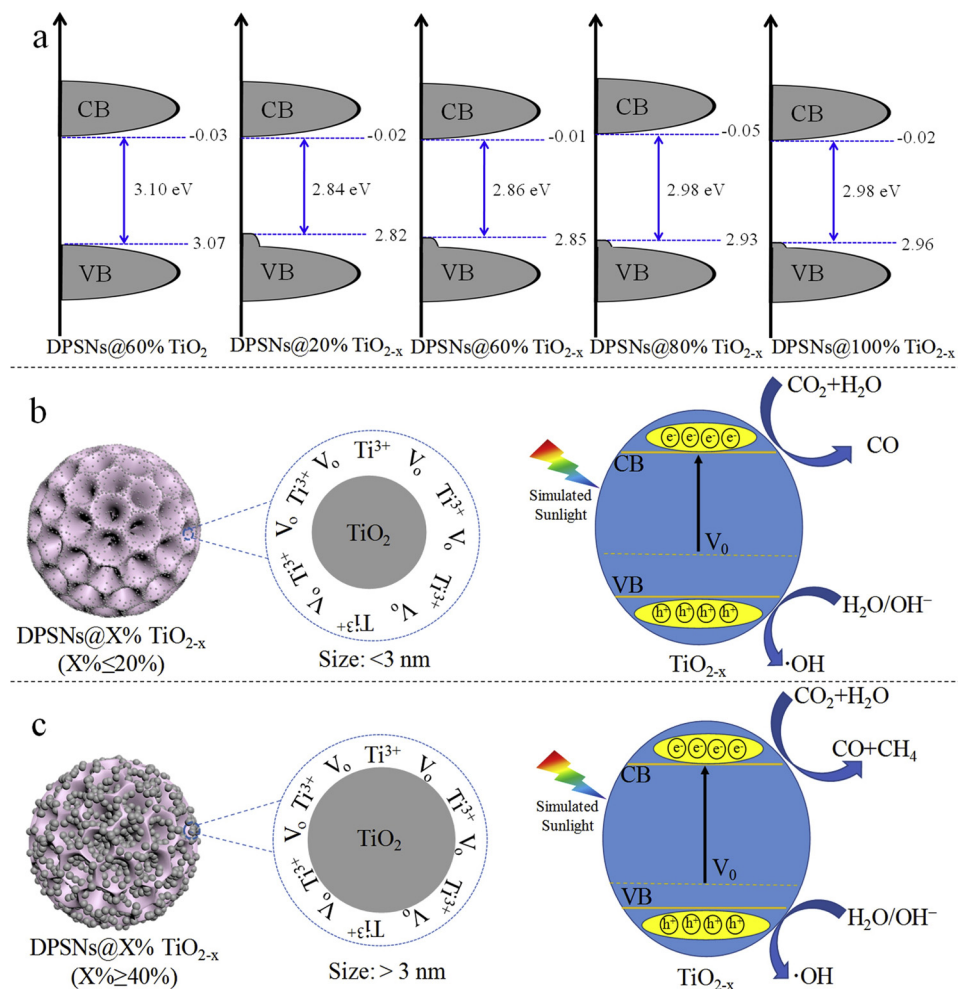


Fig. 8. (a) The proposed energy band diagrams of DPSNs@X% TiO_{2-x} in comparison with that of DPSNs@60% TiO₂ based on the bandgap (Fig. 7b) and VB (Fig. 7e). (b,c) Possible mechanism of different photocatalytic activity and selectivity of DPSNs@X% TiO_{2-x} NPs with varied particle sizes of black TiO_{2-x} NPs. Noteworthily, 1–3 nm of smaller TiO_{2-x} NPs have higher reduction degree during H₂ thermal reduction treatment, thus resulting in higher decrease of bandgap. Thus, it increases the vis-NIR light absorption ability. However, it also weakens the reduction power of electrons, which stops the kinetics of the reduction reaction from CO₂ to CH₄ involving eight electrons.

difficult to form than V_o [29].

PL emission spectrum is a useful method to investigate the recombination efficiency of photogenerated electrons and holes. The PL spectra in Fig. 7f show that the PL peak intensity of DPSNs@80% TiO_{2-x} is obviously lower than that of DPSNs@80% TiO₂, which indicates that DPSNs@80% TiO_{2-x} has a much lower recombination rate of electrons and holes under light irradiation [61,62], which favors higher photocatalytic activity. Furthermore, nanosecond-level time-resolved fluorescence decay spectrum was performed to study the transfer dynamics of photo-excited charge carrier. As exhibited in time-resolved fluorescence decay spectra of Fig. 7g, the lifetimes are 113.9 ns for DPSNs@60% TiO₂, 249.1 ns for DPSNs@60% TiO_{2-x} and 720.1 ns for DPSNs@80% TiO_{2-x}. The prolonged lifetime indicates that the efficiencies of the carrier transfer and separation in black TiO_{2-x} are greatly enhanced, thus the photoexcited charge carriers are more prone to be involved in the redox reactions instead of recombination [63].

The adsorption capacity of CO₂ on the catalyst is an important factor that determining CO₂ photoreduction performance. The CO₂ adsorption isotherms in Fig. 7h show that the maximum values at atmospheric pressure (75 °C) are 4.8 cm³ g⁻¹ for DPSNs@60% TiO_{2-x} and 4.4 cm³ g⁻¹ for DPSNs@80% TiO_{2-x} at P/P₀ = 0.96, which is approximately twice as much as that of DPSNs@60% TiO₂. The higher CO₂ adsorption capacity should result from adsorption on under-coordinated sites from V_o, which are responsible for capturing and activating CO₂ [64].

In situ DRIFTS was used to examine the adsorption and chemical activation of CO₂ molecules and analyze key intermediates for exploring the possible reaction pathway. As shown in Fig. S14, for

DPSNs@10% TiO_{2-x}, only two IR peaks appear after exposure of TiO₂ to the CO₂ and H₂O vapor, which should be ascribed to the adsorbed m-CO₃²⁻ (weak peak), and CO₂ and b-CO₃²⁻ (strong peak). Compared with DPSNs@10% TiO_{2-x}, DPSNs@80% TiO_{2-x} show much more IR peaks under no light illumination, which should be attributed to the adsorbed CO₂, m-CO₃²⁻, b-CO₃²⁻, c-CO₃²⁻, and HCO₃⁻ [65–68]. After irradiated by 300 W Xe lamp, H₂O IR peak disappears at 1173 cm⁻¹ [65]. In addition, IR peaks of m-CO₃²⁻ and b-CO₃²⁻ shift from 1378 to 1388 cm⁻¹, and from 1338 to 1342 cm⁻¹, respectively. The reason for these slight shifts to higher wave numbers is still unclear up to now, and it may be explained by the slightly decreased interaction between m-CO₃²⁻ (b-CO₃²⁻) species and TiO_{2-x} surface under Xe lamp irradiation. The peak intensity of HCO₃⁻ increases with prolonged exposure time, while the peak intensity of CO₂⁻ changes a little. The HCO₃⁻ and CO₂⁻ are usually regarded as the intermediate of CH₄ and CO [68]. It should be pointed out that the characteristic peak of CH₄ was undetectable due to its nonpolar property. These differences of intermediates can explain the huge distinction in CO₂ photocatalytic activity and selectivity between DPSNs@10% TiO_{2-x} and DPSNs@80% TiO_{2-x}.

Possible mechanism is provided to clarify different photocatalytic activity and selectivity of DPSNs@X% TiO_{2-x} NPs with varied particle sizes of black TiO_{2-x} NPs. The dependences of the morphology, geometric features, and electronic properties on the sizes of TiO_{2-x} NPs have been carefully demonstrated, as exhibited above. As shown in Fig. 8a, based on the analysis of bandgap (Fig. 7b) and VB (Fig. 7e), the energy band diagrams of DPSNs@X% TiO_{2-x} are proposed in comparison with that of DPSNs@60% TiO₂. The V_o-induced VB mid-gap tail states are labeled in diagrams. Moreover, 1–3 nm of smaller TiO_{2-x} NPs

should have higher reduction degree compared with 3–12 nm of TiO_{2-x} NPs during H_2 thermal reduction treatment (Fig. 8b,c), resulting in bigger decrease of optical bandgap. Thus, it increases the vis-NIR light absorption ability. However, it also weakens the reduction power of photogenerated electrons [27–29], which stops the kinetics of the reduction reaction from CO_2 to CH_4 involving eight electrons. It is therefore highly desirable to seek for an optimal balance between light absorption ability and electron reduction power. Based on the above characterization and analysis results, the outstanding CO_2 photoreduction performance (Fig. 5) of DPSNs@80% TiO_{2-x} should be attributed to high accessible active surface areas and suitable optical bandgap. On the one hand, high density of TiO_{2-x} NPs are well-dispersed on the surface of DPSNs@80% TiO_{2-x} , and they have appropriate particle sizes of 8–12 nm and suitable reduction degree (i.e., Vo and Ti^{3+} content). On the other hand, even at such a high X% of 80%, DPSNs@80% TiO_{2-x} still maintain high specific surface area of $208 \text{ m}^2 \text{ g}^{-1}$ due to center-radial large pore structures of DPSNs. These combined features improve CO_2 adsorption capacity (Fig. 7i), suppress recombination rate of photogenerated electrons and holes (Fig. 7g), and enhance carrier transfer and separation in black TiO_{2-x} (Fig. 7h), thus significantly enhancing CO_2 photoreduction activity (CH_4 and CO production rates: 124.3 and $14.7 \mu\text{mol g}^{-1} \text{ h}^{-1}$) (Fig. 5f). In addition, it is very interesting to achieve high selectivity (89.4%) for CH_4 , rather than CO. The exact reason is unclear, but it may result from Vo -induced suitable bandgap (2.98 eV) with -0.05 eV of CB edge (Fig. 8a), which not only can improve the photon utilization efficiency, but also can maintain the reduction power of photogenerated electrons. Moreover, the Vo defective sites on TiO_{2-x} surface could enhance the adsorption and activation of CO_2 molecules, and thus efficiently lower the reaction barrier of CO_2/CH_4 [26–31].

4. Conclusions

In this work, in order to simultaneously achieve high accessible active surface areas and regulate suitable optical bandgap, we successfully fabricated a series of porous DPSNs@X% TiO_{2-x} composite photocatalysts with tunable sizes of black TiO_{2-x} NPs from 1–2 nm to 9–12 nm, via heterogeneous interface growth followed by H_2 thermal reduction treatment. The sizes of black TiO_{2-x} NPs played a significant role in determining the physicochemical properties of DPSNs@X% TiO_{2-x} and subsequent CO_2 photocatalytic performance. Among them, DPSNs@80% TiO_{2-x} exhibited ultrahigh CH_4 production rate of $124.3 \mu\text{mol g}^{-1} \text{ h}^{-1}$, moderate CO production rate of $14.7 \mu\text{mol g}^{-1} \text{ h}^{-1}$ and high photocatalytic stability. Even at such a high X% of 80%, DPSNs@80% TiO_{2-x} still maintain high specific surface area and certain center-radial large pores, and the TiO_{2-x} NPs on the surface of DPSNs@80% TiO_{2-x} have appropriate particle sizes, good dispersion, and suitable reduction degree (i.e., Vo and Ti^{3+}). These characteristics result in higher CO_2 adsorption capacity, much lower recombination rate of photogenerated electrons and holes, enhanced carrier transfer and separation in black TiO_{2-x} NPs, thus showing remarkably high CO_2 photoreduction activity. To the best of our knowledge, such smart design has not been reported for high efficient CO_2 photoreduciton in the literatures up to now. Furthermore, this study may provide some inspiration for photocatalyst design by improving accessible active surface areas and tuning optical bandgap.

Acknowledgements

This work was supported by Fundamental Research Funds for the Central Universities (Grant No. 2302015-06500017, FRF-BR-17-032A, FRF-BR-17-002B, FRF-BD-17-016A), National Natural Science Foundation of China (Grant No. 21501009), and Beijing Municipal Science and Technology Commission (z131102002813058).

Appendix A. Supplementary data

Supplementary material related to this article can be found, in the online version, at doi:<https://doi.org/10.1016/j.apcatb.2019.117768>.

References

- [1] W.G. Tu, Y. Zhou, Z.G. Zou, *Adv. Mater.* 26 (2014) 4607–4626.
- [2] S. Sato, T. Arai, T. Morikawa, *Inorg. Chem.* 54 (2015) 5105–5113.
- [3] Y. Izumi, *Coord. Chem. Rev.* 257 (2013) 171–186.
- [4] M. Marszewski, S. Cao, J. Yu, M. Jaroniec, *Mater. Horiz.* 2 (2015) 261–278.
- [5] Z. Sun, N. Talreja, H. Tao, J. Texter, M. Muhler, J. Strunk, J. Chen, *Angew. Chem. Int. Ed.* 57 (2018) 7610–7627.
- [6] W.H. Wang, Y. Hineda, J.T. Muckerman, G.F. Manbeck, E. Fujita, *Chem. Rev.* 115 (2015) 12936–12973.
- [7] A.D. Tjandra, J. Huang, *Chin. Chem. Lett.* 29 (2018) 734–746.
- [8] K. Li, B. Peng, T. Peng, *ACS Catal.* 6 (2016) 7485–7527.
- [9] S.R. Lingampalli, M.M. Ayyub, C.N.R. Rao, *ACS Omega* 2 (2017) 2740–2748.
- [10] H. Huang, S. Tu, C. Zeng, T. Zhang, A.H. Reshak, Y. Zhang, *Angew. Chem. Int. Ed.* 56 (2017) 11860–11864.
- [11] H. Yu, J. Li, Y. Zhang, S. Yang, K. Han, F. Dong, T. Ma, H. Huang, *Angew. Chem. Int. Ed.* 58 (2019) 3880–3884.
- [12] F. Chen, H. Huang, L. Ye, T. Zhang, Y. Zhang, X. Han, T. Ma, *Adv. Funct. Mater.* 28 (2018) 1804284.
- [13] Y. Bai, I. Mora-Seró, F. De Angelis, J. Bisquert, P. Wang, *Chem. Rev.* 114 (2014) 10095–10130.
- [14] Y. Ma, X. Wang, Y. Jia, X. Chen, H. Han, C. Li, *Chem. Rev.* 114 (2014) 9987–10043.
- [15] J. Schneider, M. Matsuoka, M. Takeuchi, J. Zhang, Y. Horiuchi, M. Anpo, D.W. Bahnemann, *Chem. Rev.* 114 (2014) 9919–9986.
- [16] L. Liu, X. Chen, *Chem. Rev.* 114 (2014) 9890–9918.
- [17] M. Kapilashrami, Y. Zhang, Y.S. Liu, A. Hagfeldt, J. Guo, *Chem. Rev.* 114 (2014) 9662–9707.
- [18] M. Dahl, Y. Liu, Y. Yin, *Chem. Rev.* 114 (2014) 9853–9889.
- [19] J. Prakash, S. Sun, H.C. Swart, R.K. Gupta, *Appl. Mater. Today* 11 (2018) 82–135.
- [20] S.N. Habersreutinger, L. Schmidt-Mende, J.K. Stolarczyk, *Angew. Chem. Int. Ed.* 52 (2013) 7372–7408.
- [21] W. Li, Z. Wu, J. Wang, A.A. Elzatahry, D. Zhao, *Chem. Mater.* 26 (2014) 287–298.
- [22] S. Bagheri, Z.A.M. Hir, A.T. Yousefi, S.B.A. Hamid, *Microporous Mesoporous Mater.* 218 (2015) 206–222.
- [23] R. Zhang, A.A. Elzatahry, S.S. Al-Deyab, D. Zhao, *Nano Today* 7 (2012) 344–366.
- [24] A.A. Ismail, D.W. Bahnemann, *J. Mater. Chem.* 21 (2011) 11686–11707.
- [25] J.L. Vivero-Escoto, Y.D. Chiang, K.C.-W. Wu, Y. Yamauchi, *Sci. Technol. Adv. Mater.* 13 (2012) 013003.
- [26] X. Chen, L. Liu, F. Huang, *Chem. Soc. Rev.* 44 (2015) 1861–1885.
- [27] K. Zhang, J.H. Park, *J. Phys. Chem. Lett.* 8 (2017) 199–207.
- [28] Y. Liu, L. Tian, X. Tan, X. Li, X. Chen, *Sci. Bull.* 62 (2017) 431–441.
- [29] X. Liu, G. Zhu, X. Wang, X. Yuan, T. Lin, F. Huang, *Adv. Energy Mater.* 6 (2016) 1600452.
- [30] S. Selcuk, X. Zhao, A. Selloni, *Nat. Mater.* 17 (2018) 923–928.
- [31] S.G. Ullatil, S.B. Narendranath, S.C. Pillai, P. Periyat, *Chem. Eng. J.* 343 (2018) 708–736.
- [32] R. Asahi, T. Morikawa, H. Irie, T. Ohwaki, *Chem. Rev.* 114 (2014) 9824–9852.
- [33] M. Pelaez, N.T. Nolan, S.C. Pillai, M.K. Seery, P. Falaras, A.G. Kontos, P.S.M. Dunlop, J.W.J. Hamilton, J. Anthony Byrne, K. O’Shea, M.H. Entezari, D.D. Dionysiou, *Appl. Catal. B-Environ.* 125 (2012) 331–349.
- [34] O. Ola, M.M. Maroto-Valer, *J. Photochem. Photobiol. C* 24 (2015) 16–42.
- [35] W. Fang, M. Xing, J. Zhang, *J. Photochem. Photobiol. C* 24 (2015) 16–42.
- [36] J. Low, B. Cheng, J. Yu, *Appl. Surf. Sci.* 392 (2017) 658–686.
- [37] X. Du, S. Qiao, *Small* 11 (2015) 392–413.
- [38] A. Maity, V. Polshettiwar, *ChemSusChem* 10 (2017) 3866–3913.
- [39] X. Du, J. He, *Nanoscale* 4 (2011) 852–859.
- [40] M. Dhiman, B. Chalke, V. Polshettiwar, *J. Mater. Chem. A* 5 (2017) 1935–1940.
- [41] R. Singh, R. Belgamwar, M. Dhiman, V. Polshettiwar, *J. Mater. Chem. B* 6 (2018) 1600–1617.
- [42] Z. Wang, K.J. Balkus Jr., *Microporous Mesoporous Mater.* 243 (2017) 76–84.
- [43] Z. Wang, A.T. Brown, K. Tan, Y.J. Chabal, K.J. Balkus Jr., *J. Am. Chem. Soc.* 140 (2018) 14735–14739.
- [44] K. Zhang, L.L. Xu, J.G. Jiang, N. Calin, K.F. Lam, S.J. Zhang, H.H. Wu, G.D. Wu, B. Albelha, L. Bonneviot, P. Wu, *J. Am. Chem. Soc.* 135 (2013) 2427–2430.
- [45] Y.J. Yu, J.L. Xing, J.L. Pang, S.H. Jiang, K.F. Lam, T.Q. Yang, Q.S. Xue, K. Zhang, P. Wu, *ACS Appl. Mater. Interfaces* 6 (2014) 22655–22665.
- [46] K. Zhang, W. Zhou, X. Zhang, B. Sun, L. Wang, K. Pan, B. Jiang, G. Tian, H. Fu, *Appl. Catal. B-Environ.* 206 (2017) 336–343.
- [47] X. Zhang, W. Hu, K. Zhang, J. Wang, B. Sun, H. Li, P. Qiao, L. Wang, W. Zhou, *ACS Sustain. Chem. Eng.* 5 (2017) 6894–6901.
- [48] S. Tu, Y. Zhang, A.H. Reshak, S. Auluck, L. Ye, X. Han, T. Ma, H. Huang, *Nano Energy* 56 (2019) 840–850.
- [49] C. Zeng, H. Huang, T. Zhang, F. Dong, Y. Zhang, Y. Hu, *ACS Appl. Mater. Interfaces* 9 (2017) 27773–27783.
- [50] W. Zhou, W. Li, J.Q. Wang, Y. Qu, Y. Yang, Y. Xie, K. Zhang, L. Wang, H. Fu, D. Zhao, *J. Am. Chem. Soc.* 136 (2014) 9280–9283.
- [51] G. Yin, X. Huang, T. Chen, W. Zhao, Q. Bi, J. Xu, Y. Han, F. Huang, *ACS Catal.* 8 (2018) 1009–1017.
- [52] Y. Cao, Z. Xing, Y. Shen, Z. Li, X. Wu, X. Yan, J. Zou, S. Yang, W. Zhou, *Chem. Eng.*

J. 325 (2017) 199–207.

[53] L. Jing, W. Zhou, G. Tian, H. Fu, Chem. Soc. Rev. 42 (2013) 9509–9549.

[54] H. Song, C. Li, Z. Lou, Z. Ye, L. Zhu, ACS Sustain. Chem. Eng. 5 (2017) 8982–8987.

[55] A. Naldoni, M. Allietta, S. Santangelo, M. Marelli, F. Fabbri, S. Cappelli, C.L. Bianchi, R. Psaro, V.D. Santo, J. Am. Chem. Soc. 134 (2012) 7600–7603.

[56] X. Chen, L. Liu, P.Y. Yu, S.S. Mao, Science 331 (2011) 746–750.

[57] Y. Zhu, M.W. Shah, C. Wang, Appl. Catal. B-Environ. 203 (2017) 526–532.

[58] X. Chang, T. Wang, J. Gong, Energy Environ. Sci. 9 (2016) 2177–2196.

[59] M. Xing, Y. Zhou, C. Dong, L. Cai, L. Zeng, B. Shen, L. Pan, C. Dong, Y. Chai, J. Zhang, Y. Yin, Nano Lett. 6 (2018) 3384–3390.

[60] H. Cui, W. Zhao, C. Yang, H. Yin, T. Lin, Y. Shan, Y. Xie, H. Gu, F. Huang, J. Mater. Chem. A 2 (2014) 8612–8616.

[61] C. Dong, C. Lian, S. Hu, Z. Deng, J. Gong, M. Li, H. Liu, M. Xing, J. Zhang, Nat. Commun. 9 (2018) 1252.

[62] Z. Wang, C. Yang, T. Lin, H. Yin, P. Chen, D. Wan, F. Xu, F. Huang, J. Lin, X. Xie, M. Jiang, Adv. Funct. Mater. 23 (2013) 5444–5450.

[63] L. Hao, H. Huang, Y. Guo, Y. Zhang, ACS Sustain. Chem. Eng. 6 (2018) 1848–1862.

[64] C. Dong, M. Xing, J. Zhang, J. Phys. Chem. Lett. 7 (2016) 2962–2966.

[65] L. Liu, Y. Jiang, H. Zhao, J. Chen, J. Cheng, K. Yang, Y. Li, ACS Catal. 6 (2016) 1097–1108.

[66] A. Meng, S. Wu, B. Cheng, J. Yu, J. Xu, J. Mater. Chem. A 6 (2018) 4729–4736.

[67] L. Liu, H. Zhao, J.M. Andino, Y. Li, ACS Catal. 2 (2012) 1817–1828.

[68] H. Zhao, L. Liu, J.M. Andino, Y. Li, J. Mater. Chem. A 1 (2013) 8209–8216.